

# New Generation UV-A Filters: Understanding Their Photodynamics on a Human Skin Mimic

Temitope T. Abiola, Natércia d. N. Rodrigues, Casey Ho, Daniel J. L. Coxon, Michael D. Horbury, Josene M. Toldo, Mariana T. do Casal, Benjamin Rioux, Cédric Peyrot, Matthieu M. Mention, Patrick Balaguer, Mario Barbatti,\* Florent Allais,\* and Vasilios G. Stavros\*



Cite This: *J. Phys. Chem. Lett.* 2021, 12, 337–344



Read Online

ACCESS |



Metrics & More



Article Recommendations



Supporting Information

**ABSTRACT:** The sparsity of efficient commercial ultraviolet-A (UV-A) filters is a major challenge toward developing effective broadband sunscreens with minimal human- and eco-toxicity. To combat this, we have designed a new class of Meldrum-based phenolic UV-A filters. We explore the ultrafast photodynamics of coumaryl Meldrum, CMe, and sinapyl Meldrum (SMe), both in an industry-standard emollient and on a synthetic skin mimic, using femtosecond transient electronic and vibrational absorption spectroscopies and computational simulations. Upon photoexcitation to the lowest excited singlet state ( $S_1$ ), these Meldrum-based phenolics undergo fast and efficient nonradiative decay to repopulate the electronic ground state ( $S_0$ ). We propose an initial ultrafast twisted intramolecular charge-transfer mechanism as these systems evolve out of the Franck–Condon region toward an  $S_1/S_0$  conical intersection, followed by internal conversion to  $S_0$  and subsequent vibrational cooling. Importantly, we correlate these findings to their long-term photostability upon irradiation with a solar simulator and conclude that these molecules surpass the basic requirements of an industry-standard UV filter.



Biological systems rely on solar radiation from the Sun to provide light, warmth, and energy to sustain life.<sup>1</sup> However, excessive exposure to ultraviolet (UV) radiation from the Sun at the Earth's surface (UV-B, 280–315 nm; UV-A, 315–400 nm) causes adverse effects such as tanning (which occurs as a response to photodamage to the skin), sunburn, DNA mutations, and photoaging in humans.<sup>2–4</sup> The naturally occurring UV-absorbing pigment in human skin, melanin, often provides insufficient protection against high levels of UV radiation and sunscreens are commonly used for additional photoprotection.<sup>2</sup> While the sunscreen industry has focused on the more energetic UV-B radiation, UV-A is very abundant at the Earth's surface and penetrates deeper into the skin than UV-B.<sup>5,6</sup> Moreover, the adverse effects of overexposure of human skin to UV-A are widely reported to include DNA mutation, pigmentation, suppression of acquired immunity, and production of harmful reactive oxygen species in the skin, all of which facilitate carcinogenesis.<sup>5,7</sup> Therefore, photoprotection against UV-A radiation is of crucial importance, but it is hindered by the sparsity of approved commercial UV-A filters, as well as their lack of photostability (e.g., avobenzone).<sup>8,9</sup> In addition to being photostable, and blending into a nontoxic and aesthetically pleasing sunscreen formulation, an effective UV-filter within a sunscreen formulation should be able to dissipate the excess energy absorbed safely (i.e., without generating photoproducts) and quickly. This is both to prevent harmful side reactions and to ensure the UV-filter is “recycled” (i.e., that it returns from the electronic excited state to the electronic ground state without

detriment to its molecular integrity), to maintain photoprotection.<sup>2,10</sup>

Recently, the photodynamics of sinapoyl malate (see Figure 1), a natural UV-absorbing compound in *Arabidopsis thaliana*,<sup>11,12</sup> have been reported and found to enable efficient dissipation of absorbed energy in the form of heat, through a proposed *trans*–*cis* isomerization across the allylic bond.<sup>13,14</sup>

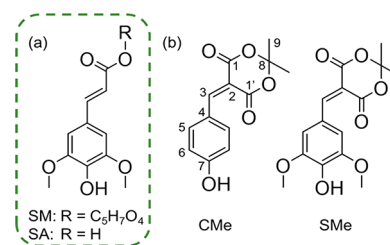


**Figure 1.** Chemical structure of (a) plant UV-filter in *Arabidopsis thaliana*, sinapoyl malate (SM), its building block sinapic acid (SA) and (b) coumaryl Meldrum (CMe) and sinapyl Meldrum (SMe) studied herein.

**Received:** October 1, 2020

**Accepted:** December 7, 2020

Furthermore, in methyl and ethyl sinapate (where R = CH<sub>3</sub> and C<sub>2</sub>H<sub>5</sub> in Figure 1a, respectively), photoexcitation to the lowest excited singlet state (S<sub>1</sub>) was found to lead to ultrafast *trans*–*cis* isomerization mediated via a conical intersection (CI) between the S<sub>1</sub> state and the electronic ground state (S<sub>0</sub>), denoted S<sub>1</sub>/S<sub>0</sub> CI.<sup>13,15–18</sup> The same CI that allows a portion of the population to isomerize, leading to the *cis*-isomer, also facilitates repopulation of the original ground state of the *trans*-isomer.<sup>15,16</sup> The *cis*-isomer of related cinnamates has been reported to possess a lower UV absorption (*i.e.*, lower extinction coefficient) and, importantly, significantly higher genotoxicity.<sup>19,20</sup> One way to circumvent concerns related to the genotoxicity of potential photoexcitation byproducts, such as geometric isomers, is to design UV-filters with identical functional groups around the allylic bond, so that isomerization results in no significant alteration of molecular structure and properties.

An example of such a symmetrically substituted UV-filter is diethyl sinapate (DES), the photodynamics of which were recently investigated.<sup>19</sup> The study showed not only that ground-state recovery of DES is very fast but also that the absorption spectrum of DES is spectrally red-shifted (further into the UV-A region) relative to its monoester building block, ethyl sinapate.<sup>19</sup> We have synthesized a new class of symmetrically substituted sinapate esters<sup>21</sup> in an attempt to further enhance UV-A absorption while maintaining the efficacy of ground-state recovery.

In this work, we present a multipronged experimental and computational study to unravel the photodynamics of a novel class of Meldrum-based phenolic UV-A filters inspired by nature, specifically CMe and SMe, shown in panel b of Figure 1, respectively. We utilize transient electronic and vibrational spectroscopies to gain unprecedented insight into the electronically excited and ground-state dynamics of these UV-A filters. Importantly, we have adapted our experimental setup to ensure that our experiment models the conditions in which these UV-A filters are found in commercial formulations (dissolved in an emollient) as closely as possible; we have deposited the bulk solution of these UV-A filters (dissolved in an emollient) on a synthetic skin mimic to model the application environment of the sunscreen. This will enable us to discern if the skin surface perturbs the dynamics of the UV-filters. As detailed further in section A of the Supporting Information (SI), we have supplemented these ultrafast experiments with ultraslow experiments, ascertaining the long-term photostability of these UV-filters when exposed to radiation from a solar simulator, as well as assessing their endocrine disruption and antioxidant properties. To complement these experiments and to better understand the dynamics of CMe and SMe, we employ high-level calculations. These reveal a new relaxation mechanism in these plant-derived UV filters involving a twisted intramolecular charge-transfer state that allows the photoexcited molecule to return to its electronic ground state with exceptionally high efficiency.

**Results. Experimental Findings.** Steady-state UV–vis absorption spectra were obtained for separate solutions of CMe and SMe in the industry-standard emollient caprylic capric triglyceride (CCT) and in ethanol. As shown in Figure 2 and SI section B, the absorption maxima ( $\lambda_{\text{max}}$ ) are located at 362 nm for CMe in CCT (denoted CMe/CCT, similarly for SMe, and in all other solutions henceforth) and 375 nm for CMe/ethanol. In the case of SMe/CCT and SMe/ethanol,  $\lambda_{\text{max}}$  is located at 396 and 407 nm, respectively. The molar

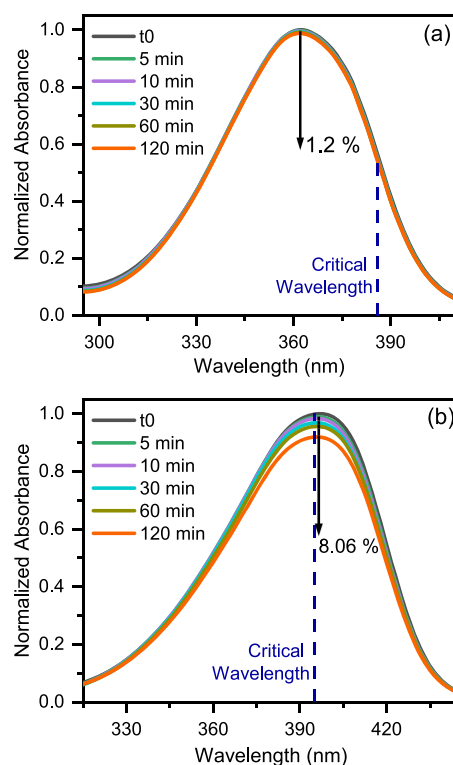


**Figure 2.** Photostability of (a) CMe and (b) SMe in CCT recorded at different intervals during irradiation with a solar simulator. The vertical dashed lines on each panel represent the position of the calculated critical wavelength of 384 and 395 nm for CMe and SMe, respectively.

extinction coefficient of CMe and SMe at their  $\lambda_{\text{max}}$  are 29 877 and 32 105 mol<sup>-1</sup> dm<sup>3</sup> cm<sup>-1</sup>, respectively, which is comparable to that of the globally most common UV-A filter, avobenzene, which has a reported molar extinction coefficient of 34 140 mol<sup>-1</sup> dm<sup>3</sup> cm<sup>-1</sup>.<sup>22</sup>

We investigated the long-term photostability of CMe and SMe in CCT, as shown in Figure 2, by collecting UV–vis spectra at various time intervals after irradiation with a solar simulator. These measurements revealed that CMe and SMe in CCT experience only a minor reduction in absorbance of less than 10% over an irradiation period of 2 h. Equivalent photostability tests could not be performed for CMe/CCT or SMe/CCT deposited on synthetic skin mimic (VITRO-CORNEUM, VC) because of excessive scattering from the sample precluding any reliable measurements. For the transient electronic absorption spectroscopy (TEAS) presented in Results, we have modified our experimental setup by increasing the pump–probe incidence angle to minimize this scattering and use off-axis parabolic mirrors to enhance collection of scattered transmitted light (see SI section A).

In addition to photostability tests, the critical wavelength (CW) of CMe and SMe was determined from the corresponding UV–vis spectra; these values are shown as a vertical dashed lines in Figure 2a,b. The CW of a UV-filter is defined as the wavelength at which the integrated area under the spectral absorbance curve reaches 90% of the total area between 290 and 400 nm.<sup>23</sup> The concept of CW in UV-A protection has been widely reported in previous literature.<sup>23–25</sup> To be labeled as broadband spectrum protection in the United States, a sunscreen must have a CW of at least 370 nm. The CW of CMe/CCT and CMe/ethanol were determined to be

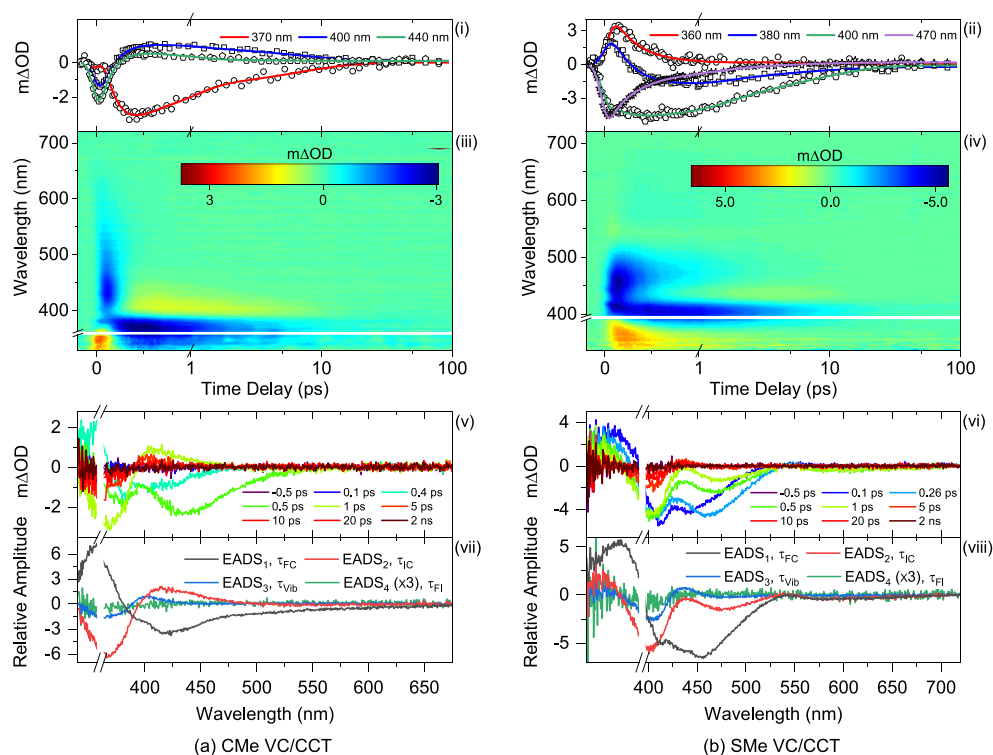


**Figure 3.** TEA spectra obtained for 20 mM (a) CMe VC/CCT photoexcited at 362 nm and (b) SMe VC/CCT photoexcited at 396 nm. The TEA spectra are presented as false color maps in panels iii and iv, respectively. The same data is presented as a line plots of  $m\Delta OD$  vs probe wavelength at selected pump–probe time delays in panels v and vi. The top panels (i and ii) show transients (raw data as symbol and fits as solid lines) at selected probe wavelengths. The bottom panels (vii and viii) show the EADS produced by the fitting procedure (see main text for details), EADS<sub>4</sub> is multiplied by three as a visual aid. The masked region of the TEA spectra, line plots, and EADS of CMe VC/CCT and SMe VC/CCT corresponds to the wavelengths for which excess scatter from the pump pulse (caused by the uneven surface of VC) interferes with data subtraction and renders the data void.

**Table 1. Summary of the Time Constants and Associated Errors Extracted from Data Collected for CMe and SMe in CCT, VC/CCT, and Ethanol with TEAS, TVAS, and Theory in Implicit Ethanol**

		TEAS			TVAS	theory
		CCT (1 mM)	VC/CCT (20 mM)	ethanol (1 mM)	ethanol (30 mM)	implicit ethanol
CMe	$\tau_{FC}$ (fs)	$220 \pm 40$	$190 \pm 40$	$190 \pm 40$	$1240 \pm 20$	$334 \pm 12^a$
	$\tau_{IC}$ (fs)	$460 \pm 40$	$450 \pm 40$	$450 \pm 40$		$628 \pm 56^a$
	$\tau_{vib}$ (ps)	$10.02 \pm 0.22$	$6.92 \pm 0.26$	$7.78 \pm 0.13$	$7.44 \pm 0.61$	
	$\tau_{FI}$ (ns)		>2		>1.5	
SMe	$\tau_{FC}$ (fs)	$300 \pm 40$	$280 \pm 40$	$350 \pm 40$		$\sim 600^b$
	$\tau_{IC}$ (ps)	$1.15 \pm 0.04$	$1.21 \pm 0.05$	$0.79 \pm 0.04$		$\sim 0.94^b$
	$\tau_{vib}$ (ps)	$8.26 \pm 0.04$	$8.69 \pm 0.43$	$4.26 \pm 0.09$	$5.06 \pm 0.08$	
	$\tau_{FI}$ (ns)	>2	>2	>2	>1.5	$5.7^c$

<sup>a</sup>Dynamics simulations of 70 trajectories. <sup>b</sup>Dynamics of 10 trajectories. <sup>c</sup>First-order perturbation theory.  $\tau_{FC}$  corresponds to the time to relax from the Franck–Condon (FC) to the twisted CT minimum;  $\tau_{IC}$  is the  $S_1/S_0$  internal conversion time;  $\tau_{vib}$  is the time for vibrational cooling in the ground state; and  $\tau_{FI}$  is the fluorescence time for a minor fraction of the population that does not undergo IC. TEA spectra time constants under other conditions are given in Table S1.

384 and 395 nm, respectively (SI Figure S2); for SMe/CCT and SMe/ethanol, the CW takes values of 395 and 396 nm, respectively (cf. 378 nm for avobenzene in ethanol<sup>19</sup>). Furthermore, endocrine disruption analysis was conducted for SMe and reported in SI section D, to supplement those already reported for CMe;<sup>21</sup> both molecules are found to be innocuous in this sense.

To elucidate the origin of the photostability of CMe and SMe, we investigated their ultrafast (femto- to picoseconds) photodynamics with TEAS. A full description of our experimental setup and procedures are detailed in SI section

A. TEAS measurements obtained for separate solutions of CMe/CCT, SMe/CCT, CMe/ethanol, and SMe/ethanol are presented in SI Figures S4 and S5 and discussed in SI section E. Presented in Figure 3 are the TEAS measurements for separate solutions of CMe/CCT and SMe/CCT at 20 mM deposited on VC (denoted CMe VC/CCT and SMe VC/CCT). The transient electronic absorption (TEA) spectra of CMe and SMe are, in all environments (CCT, ethanol, and VC), dominated by four features: First, there is a negative feature centered at  $\sim 362$  nm for CMe and  $\sim 396$  nm for SMe, attributed to a ground-state bleach (GSB) through comparison

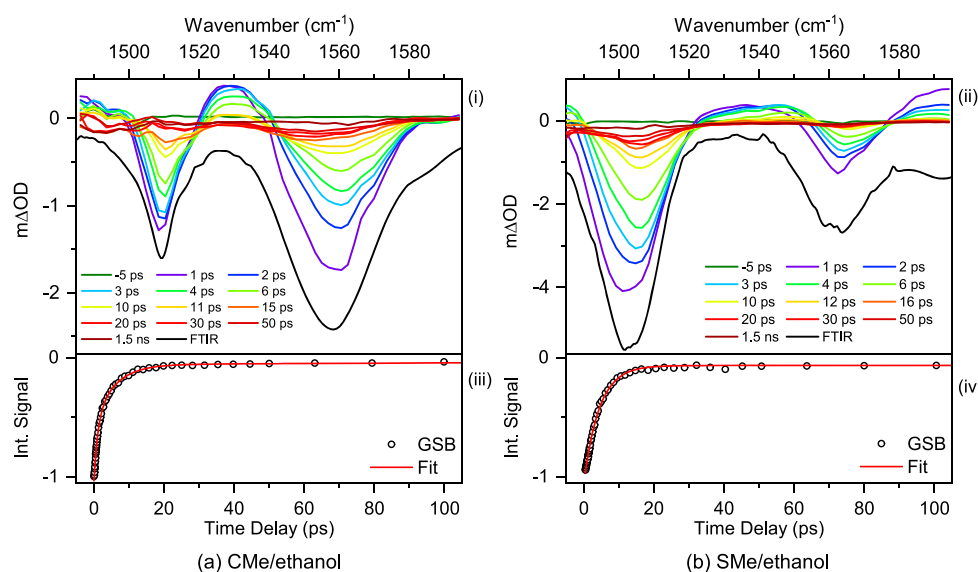


**Figure 4.** TVA spectra obtained for 30 mM solution of (a) CMe/ethanol following 375 nm excitation and (b) SMe/ethanol following 407 nm excitation, using a probe pulse centered at 1536  $\text{cm}^{-1}$ . The TVA spectra are presented as smoothed line plots of  $m\Delta\text{OD}$  vs probe wavenumber at selected pump–probe time delays in panels i and ii, respectively. The steady-state Fourier transform infrared (FTIR) spectra of CMe/ethanol and SMe/ethanol are shown as black lines in panels i and ii. The bottom panels iii and iv show the transients for the GSB recovery (raw data as open circles and fit as solid red line) of signals at selected wavenumber. For CMe/ethanol the normalized integration of the 1558  $\text{cm}^{-1}$  GSB signal was fitted with a triexponential function, while the normalized integration of the 1505  $\text{cm}^{-1}$  GSB signal was fitted with a biexponential function for SMe/ethanol. Attempt to fit CMe/ethanol data with a biexponential function returned a poor fit. Frequency calculations (see SI section J) suggest the vibrational feature probed is the allylic C=C stretching at 1558  $\text{cm}^{-1}$  and aromatic C–H bending and C=C stretching at 1505  $\text{cm}^{-1}$ .

**Table 2.** Vertical Absorption Energy into  $S_n$  ( $\Delta E_{\text{vert}}$ ), Vertical Emission Energy ( $\Delta E_{\text{em}}$ ), and Adiabatic Energy ( $\Delta E_{\text{adiab}}$ ) for CMe and SMe, Calculated with TD-DFT ( $\omega\text{B97XD}/\text{aug-cc-pVTZ}/\omega\text{B97XD}/\text{cc-pVDZ}$ ; PCM (ethanol))<sup>a</sup>

		$\Delta E_{\text{vert}}$ (eV)		$\Delta E_{\text{em}}$ (eV)		$\Delta E_{\text{ad}}$ (eV)	
CMe	$S_1$	$\pi\pi^*$	3.83 (0.8765) 3.31 <sup>b</sup>	$\pi\pi^*$	0.79 (0.0000)	$\pi\pi^*$	2.51 (0.0000)
	$S_2$	$\pi\pi^*$	4.62 (0.0074)	$n\pi^*$	3.14 (0.0321)	$\pi\pi^*$	4.25 (0.0511)
	$S_3$	$n\pi^*$	4.70 (0.0038)	$\pi\pi^*$	3.64 (0.0244)	$n\pi^*$	4.30 (0.0160)
SMe	$S_{1\text{-LE}}$	$\pi\pi^*$	3.57 (0.6662)3.05 <sup>b</sup>	$\pi\pi^*$	2.77 (0.5281)	$\pi\pi^*$	3.18 (0.5281)
	$S_{1\text{-TICT}}$			$\pi\pi^*$	0.82 (0.0000)	$\pi\pi^*$	2.49 (0.0000)
	$S_2$	$\pi\pi^*$	3.86 (0.0183)	$\pi\pi^*$	2.76 (0.0168) <sup>c</sup>		NO <sup>d</sup>
	$S_3$	$n\pi^*$	4.68 (0.0019)	$n\pi^*$	3.14 (0.0968) <sup>c</sup>	$n\pi^*$	4.29 (0.0000)

<sup>a</sup>Oscillator strengths are given in the parentheses. <sup>b</sup>Experimental values in ethanol. <sup>c</sup>Relative to  $S_{1\text{-TICT}}$  minimum. <sup>d</sup>NO: Not obtained; the state optimizes to  $S_{1\text{-FC}}$ .

with the steady-state UV–vis absorption spectra (see Figure 2a,b). A second, negative feature centered at  $\sim 450$  and  $\sim 475$  nm in CMe and SMe, respectively, is attributed to stimulated emission (SE) between the  $S_1$  ( $1^1\pi\pi^*$ ) state and the  $S_0$  state, based on our electronic structure calculations (discussed below) and the emission spectra presented in SI section F. We note, for the purpose of the discussion below, that the SE feature observed for CMe appears to decay back to baseline within  $\sim 1$  ps, while that of SMe persists up to  $\sim 5$  ps. Third, there is an intense positive feature attributed to excited-state absorption (ESA) of the  $S_1$  ( $1^1\pi\pi^*$ ) state, centered at  $\sim 365$  nm in both CMe and SMe; finally, close examination of the TEA spectra of both molecules reveals a second ESA centered at  $\sim 420$  nm, which decays on a similar time scale to the GSB and is more clearly visible in the evolution associated difference spectra (EADS) in Figure 3 and SI Figure S4. We suggest that this ESA feature results from the formation of a vibrationally hot electronic ground state following internal conversion from  $S_1$  to  $S_0$  mediated by the  $S_1/S_0$  CI.

To extract kinetic information from the TEA spectra, we carried out global fitting employing a sequential ( $A \xrightarrow{\tau_1} B \xrightarrow{\tau_2} C \xrightarrow{\tau_3} D \dots$ ) kinetic model using the Glotaran software package.<sup>26,27</sup> The extracted time constants  $\tau_n$  (where  $n$  denotes the dynamical process associated with each time constant) are shown in Table 1. The errors quoted for these fits are those produced by the fitting software; however, the quality of each fit is best evaluated by analysis of the associated residuals shown in SI section G (Figure S7). The solvent-only time-zero responses, which correspond to our instrument response, are shown in Figure S8 and discussed in SI section H.

Complementary transient vibrational absorption spectroscopy (TVAS) measurements, *i.e.*, UV-pump/infrared(IR)-probe, were obtained for CMe and SMe in order to probe changes in vibrational state on the  $S_0$  electronic surface following internal conversion from the  $S_1$  state. Because of the strong IR absorption of CCT, TVAS measurements were taken in ethanol, which we have found from TEAS measurements

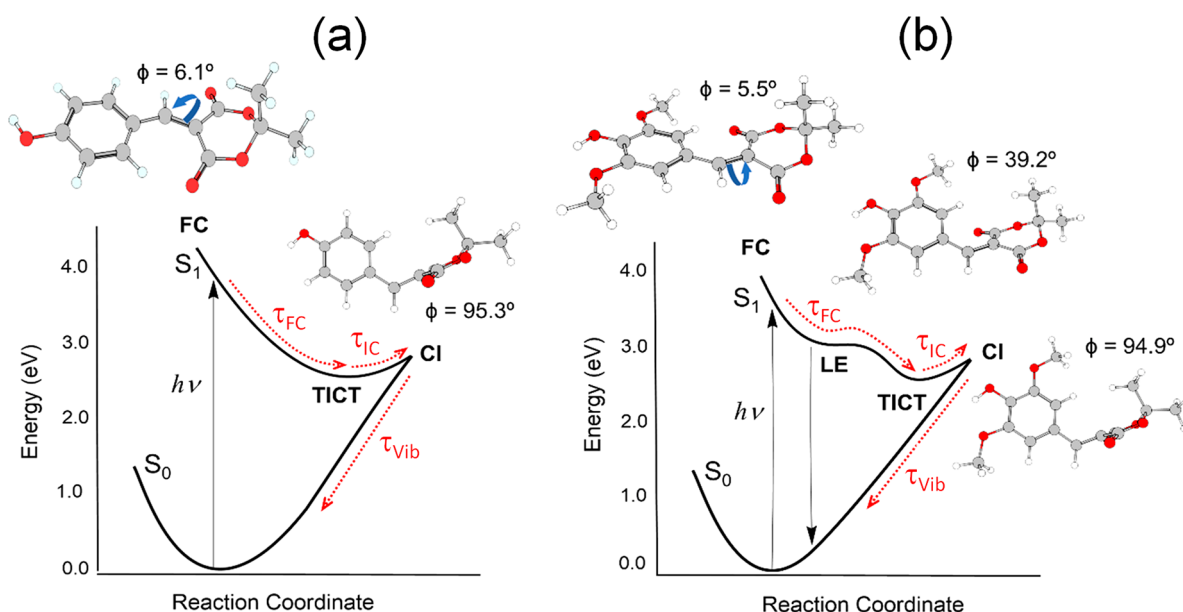


**Figure 5.** Topography of the PES for CMe (left) and SMe (right). Minima and state intersections calculated with TD-DFT at  $\omega$ B97XD/aug-cc-pVTZ// $\omega$ B97XD/cc-pVDZ level with implicit ethanol solvent, the solid lines schematically interpolate these points. Molecular conformations at the Franck–Condon (FC) region, at the global minimum ( $S_{1\text{-TICT}}$ ) and at the local  $S_{1\text{-LE}}$  minimum (only for SMe) are shown. Their twisting angles  $\phi$  (C1'–C2–C3–C4 dihedral angle) are also indicated. The molecular structures for the  $S_1/S_0$  intersection are omitted here for clarity but are shown in Figure S15; they are qualitatively similar to the  $S_{1\text{-TICT}}$  with twisting angle  $\phi = 94.8^\circ$  and  $\phi = 86.8^\circ$  for CMe and SMe, respectively.

presented in SI section E to be comparable to a CCT environment. The transient vibrational absorption (TVA) spectra for CMe and SMe are reported in Figure 4 (see SI Figure S9 for additional TVA spectra and section I for discussion). The strongest GSB features observed in the TVA spectra of CMe and SMe were fitted with triexponential (CMe) and biexponential (SMe) functions, shown in Figure 4, yielding the time constants, shown in Table 1. The fits of the GSB feature at  $1510\text{ cm}^{-1}$  for CMe and  $1558\text{ cm}^{-1}$  for SMe as well as the GSB feature at  $1714\text{ cm}^{-1}$  (reported in SI Figure S9) for both UV-filters are reported in SI Table S2.

**Computational Studies of CMe and SMe.** In interpreting experimental results, we have made use of electronic structure calculations (details in SI section J) carried out for CMe and SMe using an implicit solvation model for ethanol. The inclusion of explicit solvation does not have significant effect on the vertical excitations, although it slightly stabilizes the lowest  $\pi\pi^*$  states and destabilizes the lowest  $n\pi^*$  state (see SI Tables S3 and S4). Optimized geometries are shown in SI Figure S10, along with the initial excitation in SI Figures S11 and S12. In addition, molecular orbital characterization for the singlet states is shown in SI Figure S13 and S14. The calculated vertical excitations presented in Table 2 show that the photoexcitation at  $\lambda_{\text{max}}$  of CMe and SMe corresponds to population of the bright  $S_1$  state ( $1^1\pi\pi^*$ ). For CMe, this state has a large oscillator strength and lies below the  $1^1n\pi^*$  state ( $S_3$  state) by 0.9 eV, according to the TD- $\omega$ B97XD and CASPT2 results (see SI Table S3). This energy difference is slightly greater for SMe (1.1 eV) because of stabilization of the  $\pi\pi^*$  states arising from the electron donor methoxy groups.

Following the vertical excitation, the optimization of the  $S_1$  ( $1^1\pi\pi^*$ ),  $S_2$  ( $2^1\pi\pi^*$ ), and  $S_3$  ( $1^1n\pi^*$ ) states shows that the  $1^1\pi\pi^*$  state is largely stabilized, lying below the  $n\pi^*$  state by  $\sim 1.8$  eV for both molecules (see the adiabatic energies in Table 2). This large energy difference between the states hinders any possibility of internal conversion to a dark  $1^1n\pi^*$

state, previously reported as a competitive decay channel for other cinnamate and sinapate derivatives.<sup>12,28,29</sup> The strong stabilization of the  $S_1$  state occurs through twisting around the C2–C3 (see Figure 1) allylic bond toward a twisted intramolecular charge transfer (TICT) minimum,  $S_{1\text{-TICT}}$ , at  $\phi \approx 90^\circ$  twist (state characterization is given in SI Table S5;  $\phi$  is the C1'–C2–C3–C4 dihedral angle).

The excited-state topography of SMe and CMe revealed by the theoretical approach is schematically shown in Figure 5. While CMe shows a barrierless  $S_1$  relaxation toward the  $S_{1\text{-TICT}}$  twisted minimum, in SMe the equivalent relaxation leads to a flat region on the potential energy surface (PES), with a locally excited minimum ( $S_{1\text{-LE}}$ ) and partially twisted geometry ( $\phi \approx 40^\circ$ ). The barrier between the LE and TICT minima is less than 0.1 eV (see SI Figures S15 and S16). Near the  $90^\circ$  twisted geometry, a  $S_1/S_0$  minimum energy crossing point was found 0.2 eV (at TD-DFT) above the  $S_{1\text{-TICT}}$  minimum for both CMe and SMe (SI Figure S16). This uphill intersection was determined for both molecules using sequential penalty function adapted to TD-DFT and further confirmed by CASPT2//CASSCF calculations for CMe, which provided a 0.37 eV barrier.

To verify the time evolution of the molecules along this pathway, we performed excited-state dynamics simulations by propagating an ensemble of trajectories using TD-DFT ( $\omega$ B97XD/cc-pVDZ) in implicit ethanol until  $S_1$  reached a crossing with  $S_0$  (see SI section J-iii). The time to reach the crossing point for each trajectory was assumed to correspond to the internal conversion (IC) time. For CMe, all trajectories undergo an ultrafast twist around the allylic bond, which drives it toward the intersection with the ground state. Monitoring the dynamics starting from the vertically excited-state, we have observed that the  $S_1/S_0$  energy gap quickly drops to  $\sim 0.5$  eV with a mean time of  $334 \pm 12$  fs, when twisted geometries near  $90^\circ$  are reached (SI Figure S19), in good agreement with the experimental  $\tau_{\text{FC}}$  (see Table 1). After this gap closure, the

molecule requires a further 300 fs to reach the  $S_1/S_0$  intersection which, as we mentioned, is energetically above the  $S_{1-TICT}$  minimum. During this time, the  $S_1/S_0$  energy gap remains small ( $<0.5$  eV) and we can observe oscillations in bond lengths, ring puckering, and pyramidalization of the C3 atom (see Figure 1). The IC follows an exponential decay pattern with a mean time of  $628 \pm 56$  fs, in line with the experimentally obtained  $\tau_{IC}$  (see Table 1). For SMe, only a few trajectories with exploratory character and low statistical significance were run. For this molecule, the dynamics evolution is similar, although it is elongated to  $\sim 600$  fs because of the flat region around the  $S_{1-LE}$  minimum. Like in CMe, IC takes a further 300 fs, occurring at  $\sim 940$  fs.

We now discuss the implications of our results with regard to photoprotection, drawing on the different aspect of the experimental and computational studies. The presented UV-vis spectra, photostability, and CW tests reveal that CMe and SMe are photostable UV-A absorbers. In addition, previous studies have reported not only promising antioxidant properties for this class of molecules<sup>21</sup> but also a lack of endocrine disruption effect for the CMe.<sup>21</sup> Endocrine disruption analysis for SMe highlighted the same innocuousness (see SI section D). Together, these observations make CMe and SMe promising candidates for inclusion in commercial formulations,<sup>19</sup> although further analysis of their toxicity is needed. With regard to their ultrafast photodynamics, which should allow for fast and efficient dissipation of excess energy, we draw on our experimental results, calculations, and previous related studies to assign dynamical processes to extracted time constants and to discuss the implications of our findings.

Previous studies on related systems have shown that, following initial photoexcitation to the  $1^1\pi\pi^*$  state, these molecules tend to undergo rapid geometry and vibrational relaxation out of the Franck–Condon region, usually evidenced by slight changes in the EADS.<sup>13,16,19</sup> While we might expect CMe and SMe to undergo a similar dynamical process, the EADS associated with  $\tau_{FC}$  (EADS<sub>1</sub>) is significantly different from EADS<sub>2</sub> (see Figure 3). This marked difference suggests either a change of state or excited-state population migration to a drastically different region of the PES. Indeed, our calculations reveal that the relaxation of the initially excited  $1^1\pi\pi^*$  state of both CMe and SMe follows a large energy stabilization alongside a marked geometrical change. As indicated in Figure 5, the  $1^1\pi\pi^*$  state evolves into a global minimum with a geometry twisted  $\sim 90^\circ$  around the allylic double bond and large charge-transfer character prior to reaching a CI with the ground state. TICT processes have been previously reported for systems in which electron withdrawing and donating substituents are positioned *para* to each other (*i.e.*, position 1 and 4 on the benzene ring), lending further support to our hypothesis.<sup>30–32</sup> Hence, we assign  $\tau_{FC}$  for CMe and SMe (see Table 1), to an ultrafast relaxation into the TICT minimum ( $S_{1-TICT}$ ). Once this minimum is reached, we propose that IC takes place from the TICT to the ground state within the time scale of  $\tau_{IC}$ . These assignments of  $\tau_{FC}$  and  $\tau_{IC}$  are confirmed by the results of our excited-state dynamic simulations, which yield times for movement out of the Franck–Condon region that are in excellent agreement with experimental  $\tau_{FC}$  values (see Table 1).

In addition, the time constants associated with the recovery of GSB features in the TVA spectra effectively correspond to the rate of vibrational cooling of the vibrationally hot  $S_0$ , as previously described for other systems.<sup>33,34</sup> The first time

constant ( $\sim 1$  ps) extracted from the fit to each GSB feature of the TVA spectra in CMe, as well as the GSB feature of SMe at  $1714\text{ cm}^{-1}$ , encompasses several initial processes, including solvent heating and any overlapping features. Consequently, we refrain from conclusive assignment of this time constant in these cases. However,  $\tau_{vib}$  for CMe and SMe from their TVA spectra match the equivalent  $\tau_{vib}$  values in TEA spectra in ethanol (see Table 1):  $\tau_{vib} \approx 8$  ps observed for CMe in TVA spectra and TEA spectra, and  $\tau_{vib} \approx 5$  ps in TVA spectra and  $\sim 4$  ps in TEA spectra for SMe. This agreement confirms our assignment of  $\tau_{vib}$  for CMe and SMe in TEA spectra (in both ethanol and CCT) to vibrational cooling within their respective  $S_0$  states.

Finally, the remaining time constant extracted from the TVA spectra,  $\tau_{FI}$ , is associated with the residual GSB feature observable in the EADS of both CMe and SMe. This feature persists beyond the 2 ns temporal window of our experiments, with  $<1\%$  of the feature's intensity remaining (see SI Figure S20). The linear power dependence observed for these measurements (see SI section L, Figure S21) suggests that it does not correspond to radical formation, which has previously been attributed to a two-photon ionization mechanism.<sup>13,35</sup> We address this incomplete recovery of the ground state by once again considering the results of our electronic structure calculations: as discussed, the only difference between the potential energy profiles of CMe and SMe is the partially twisted LE minimum in the  $S_1$  state of SMe. Although this minimum has a small energy barrier ( $<0.1$  eV), we show in SI section J-iv that a small fraction of the SMe population could be trapped in the  $S_{1-LE}$  minimum long enough to fluoresce at 448 nm emission, within 5.7 ns (in reasonable agreement with the TEAS result in ethanol, 475 nm in  $>2$  ns). We note, however, that the absence of an SE feature beyond 5 ps and up to 2 ns in the TEA spectra could simply reflect the small amount of trapped population in the  $S_{1-LE}$  state, leading to a weak SE that is within the signal-to-noise of the TEA spectra. For CMe, although we do not observe  $S_{1-LE}$  minimum on the PES, a small fraction of the population could be trapped within the shallow TICT minimum or some other state not captured by our calculation, which could explain the incomplete recovery of the GSB feature in EADS<sub>4</sub>, clearly visible in the 2 ns TEA spectrum in SI Figure S20. An alternative relaxation pathway for the long-lived species (represented by  $\tau_{FI}$ ) could be intersystem crossing (ISC) from the  $S_1$  to triplet state. However, we are unable to confirm or rule out either mechanism; the weak fluorescence emission from CMe and SMe has precluded us from ascertaining any reasonable fluorescence lifetime measurements. Independently of the  $\tau_{FI}$  assignment, it is crucial to note that additional TEAS measurements, NMR and HPLC measurements presented in SI Figures S22–S24 lead us to confidently conclude that the long-lived  $\tau_{FI}$  is not likely to be the result of interaction with the skin mimic, nor is it associated with the formation of any potentially harmful photoproduct in either CMe or SMe.

In summary, combining ultrafast transient absorption spectroscopy, excited-state calculations, and steady-state studies, we have provided unprecedented insight into the excited-state photodynamics of CMe and SMe in closer-to-real environments (*i.e.*, in industrial grade emollient and on skin mimic surface, providing more than just conventional solvent–chromophore interaction). Following photoexcitation of CMe and SMe to their respective  $S_1$  states (in either bulk ethanol or CCT, or deposited on a skin mimic), our results reveal fast

relaxation involving TICT followed by IC to the  $S_0$  state and vibrational cooling on the ground-state surface. Finally, we note a mild incomplete ground-state recovery within 2 ns, which we assigned to excited-state population trapped at a locally excited minimum. Steady-state studies revealed that these molecules are highly photostable over prolonged irradiation, surpassing the most widely used UV-A filter on the market (avobenzone). These studies also demonstrate that these filters do not produce any observable photoproducts after two hours of simulated solar irradiation (see [SI section M](#)). Importantly, our results showed that the dynamics of CMe and SMe are, at best, mildly influenced by environment following our studies in ethanol, emollient, and on a skin mimic. Allied to the strong UV-A protection they afford and the favorable antioxidant and endocrine disruption tests,<sup>21</sup> CMe and SMe present as highly promising candidates for inclusion in commercial sunscreen formulations.

Given the importance of structure–dynamics–function relationships in a multitude of fields, including the present studies linked to sunscreen science, our work clearly demonstrates that the dynamics of CMe and SMe UV-filters are only mildly influenced by surrounding environment (solution versus skin mimic). Coupled to the demonstration that symmetrical substitution across the allylic bond circumvents the formation of potentially toxic geometric isomer photoproducts, our nature-inspired UV-filters offer a promising avenue of photon-to-molecule heat generation. This has ramifications, not just to researchers within the sunscreen industry, but also to researchers whose work targets, more broadly, photon-to-molecule energy conversion, such as light capturing for solar fuels, light-driven catalyst for fine chemicals, and fluorophores with environment-specific emission for medical imaging.

## ■ ASSOCIATED CONTENT

### SI Supporting Information

The Supporting Information is available free of charge at <https://pubs.acs.org/doi/10.1021/acs.jpcllett.0c03004>.

Experimental methods; photostability measurements of CMe and SMe in ethanol; critical wavelength of CMe and SMe in ethanol; endocrine disruption measurements of SMe; additional TEAS measurements of CMe/CCT, SMe/CCT, CMe/ethanol, and SMe/ethanol at 1 mM concentration; emission spectra of CMe and SMe in ethanol; residuals between fits returned by sequential fit and raw data for CMe and SMe in CCT and VC/CCT; instrument response; TVAS experimental setup and additional data; pump power dependence study; TEAS measurements of CMe/CCT and SMe/CCT at higher concentration; <sup>1</sup>H NMR of pre- and post-irradiated CMe and SMe; HPLC chromatogram of pre- and post-irradiated CMe and SMe on VC; kinetic fits; further description of methodology; vertical and adiabatic energies at different levels of theory; optimized structures; representative trajectories; analysis of fluorescence in SMe ([PDF](#))

## ■ AUTHOR INFORMATION

### Corresponding Authors

**Mario Barbatti** – Aix Marseille University, CNRS, ICR, Marseille, France; [orcid.org/0000-0001-9336-6607](https://orcid.org/0000-0001-9336-6607); Email: [mario.barbatti@univ-amu.fr](mailto:mario.barbatti@univ-amu.fr)

**Florent Allais** – URD Agro-Biotechnologies (ABI), CEBB, AgroParisTech, 51110 Pomacle, France; [orcid.org/0000-0003-4132-6210](https://orcid.org/0000-0003-4132-6210); Email: [florent.allais@agroparistech.fr](mailto:florent.allais@agroparistech.fr)  
**Vasilios G. Stavros** – Department of Chemistry, University of Warwick, Coventry CV4 7AL, United Kingdom; [orcid.org/0000-0002-6828-958X](https://orcid.org/0000-0002-6828-958X); Email: [v.stavros@warwick.ac.uk](mailto:v.stavros@warwick.ac.uk)

### Authors

**Temitope T. Abiola** – Department of Chemistry, University of Warwick, Coventry CV4 7AL, United Kingdom  
**Natércia d. N. Rodrigues** – Department of Chemistry, University of Warwick, Coventry CV4 7AL, United Kingdom  
**Casey Ho** – Department of Chemistry, University of Warwick, Coventry CV4 7AL, United Kingdom  
**Daniel J. L. Coxon** – Department of Chemistry and Department of Physics, University of Warwick, Coventry CV4 7AL, United Kingdom; EPSRC Centre for Doctoral Training in Diamond Science and Technology, Coventry, United Kingdom  
**Michael D. Horbury** – School of Electrical and Electronic Engineering, University of Leeds, Leeds LS2 9JT, United Kingdom  
**Josene M. Toldo** – Aix Marseille University, CNRS, ICR, Marseille, France; [orcid.org/0000-0002-8969-6635](https://orcid.org/0000-0002-8969-6635)  
**Mariana T. do Casal** – Aix Marseille University, CNRS, ICR, Marseille, France  
**Benjamin Rioux** – URD Agro-Biotechnologies (ABI), CEBB, AgroParisTech, 51110 Pomacle, France  
**Cédric Peyrot** – URD Agro-Biotechnologies (ABI), CEBB, AgroParisTech, 51110 Pomacle, France; [orcid.org/0000-0001-8843-6498](https://orcid.org/0000-0001-8843-6498)  
**Matthieu M. Mention** – URD Agro-Biotechnologies (ABI), CEBB, AgroParisTech, 51110 Pomacle, France; [orcid.org/0000-0002-2309-9870](https://orcid.org/0000-0002-2309-9870)  
**Patrick Balaguer** – IRCM, Inserm, Univ. Montpellier, ICM, Montpellier, France

Complete contact information is available at: <https://pubs.acs.org/doi/10.1021/acs.jpcllett.0c03004>

### Notes

The authors declare no competing financial interest. The datasets presented in this study can be found in online repositories. The names of the repository/repositories and accession number(s) can be found below: Zenodo repository DOI: 10.5281/zenodo.4321973.

## ■ ACKNOWLEDGMENTS

The authors acknowledge the support of the FetOpen grant BoostCrop (Grant Agreement 828753). The authors thank the Warwick Centre for Ultrafast Spectroscopy (WCUS) for the use of transient vibrational absorption spectroscopy (TVAS) and Fluorolog 3. T.T.A. thanks The University of Warwick for Ph.D. studentship through the Chancellor Scholarship. M.D.H. thanks the Leverhulme Trust for postdoctoral funding. M.T. do C., J.M.T., and M.B. thank the project Equip@Meso (ANR-10-EQPX-29-01) funded by the French Government “Investissements d’Avenir” program for the computational resources. B.R., C.P., M.M.M., and F.A. thank the Agence Nationale de la Recherche (Grant Number ANR-17-CE07-0046), as well as the Grand Reims, Conseil Départemental de la Marne, and the Grand Est region for financial support. V.G.S. thanks the Royal Society and Leverhulme Trust for a Royal Society Leverhulme

Trust Senior Research Fellowship, the EPSRC (UK) under Grant EP/N010825/1 and EPSRC and the De Beers Group facilitated through the Center for Doctoral Training in Diamond Science and Technology. The authors thank Nikola Chmel, Abigail Whittock, and Michael Staniforth for their help and useful discussion.

## REFERENCES

- (1) Ahmed, F. K.; Lim, H. W.; Draeos, Z. D. Worldwide regulation of UV filters: Current status and future trends. In *Clinical Guide to Sunscreens and Photoprotection*; Informa Healthcare: New York, 2009; pp 65–81.
- (2) Baker, L. A.; Marchetti, B.; Karsili, T. N. V.; Stavros, V. G.; Ashfold, M. N. R. Photoprotection: Extending lessons learned from studying natural sunscreens to the design of artificial sunscreen constituents. *Chem. Soc. Rev.* **2017**, *46*, 3770–3791.
- (3) Rodrigues, N. D. N.; Cole-Filipiak, N. C.; Horbury, M. D.; Staniforth, M.; Karsili, T. N. V.; Peperstraete, Y.; Stavros, V. G. Photophysics of the sunscreen ingredient menthyl anthranilate and its precursor methyl anthranilate: A bottom-up approach to photoprotection. *J. Photochem. Photobiol., A* **2018**, *353*, 376–384.
- (4) Dahle, J.; Kvam, E. Induction of delayed mutations and chromosomal instability in fibroblasts after UVA-, UVB-, and X-radiation. *Cancer Res.* **2003**, *63*, 1464–1469.
- (5) Battie, C.; Jitsukawa, S.; Bernerd, F.; Del Bino, S.; Marionnet, C.; Verschoore, M. New insights in photoaging, UVA induced damage and skin types. *Exp. Dermatol.* **2014**, *23*, 7–12.
- (6) Brenner, M.; Hearing, V. The protective role of melanin against UV damage in human skin. *Photochem. Photobiol.* **2008**, *84*, 539–549.
- (7) Matsumura, Y.; Ananthaswamy, H. N. Molecular mechanisms of photocarcinogenesis. *Front. Biosci.* **2002**, *7*, d765–783.
- (8) Afonso, S.; Horita, K.; Sousa e Silva, J. P.; Almeida, I. F.; Amaral, M. H.; Lobão, P. A.; Costa, P. C.; Miranda, M. S.; da Silva, J. C. G. E.; Lobo, J. M. S. Photodegradation of avobenzonone: stabilization effect of antioxidants. *J. Photochem. Photobiol., B* **2014**, *140*, 36–40.
- (9) Mturi, G. J.; Martincigh, B. S. Photostability of the suncreening agent 4-tert-butyl-4'-methoxydibenzoylmethane (avobenzonone) in solvents of different polarity and proticity. *J. Photochem. Photobiol., A* **2008**, *200*, 410–420.
- (10) Rodrigues, N. D. N.; Staniforth, M.; Stavros, V. G. Photophysics of sunscreen molecules in the gas phase: a stepwise approach towards understanding and developing next-generation sunscreens. *Proc. R. Soc. London, Ser. A* **2016**, *472*, 20160677.
- (11) Fraser, C. M.; Chapple, C. The phenylpropanoid pathway in Arabidopsis. *Arabidopsis Book/American Society of Plant Biologists* **2011**, *9*.
- (12) Dean, J. C.; Kusaka, R.; Walsh, P. S.; Allais, F.; Zwier, T. S. Plant sunscreens in the UV-B: ultraviolet spectroscopy of jet-cooled sinapoyl malate, sinapic acid, and sinapate ester derivatives. *J. Am. Chem. Soc.* **2014**, *136*, 14780–14795.
- (13) Baker, L. A.; Horbury, M. D.; Greenough, S. E.; Allais, F.; Walsh, P. S.; Habershon, S.; Stavros, V. G. Ultrafast photoprotecting sunscreens in natural plants. *J. Phys. Chem. Lett.* **2016**, *7*, 56–61.
- (14) Luo, J.; Liu, Y.; Yang, S.; Flourat, A. L.; Allais, F.; Han, K. Ultrafast barrierless photoisomerization and strong ultraviolet absorption of photoproducts in plant sunscreens. *J. Phys. Chem. Lett.* **2017**, *8*, 1025–1030.
- (15) Baker, L. A.; Staniforth, M.; Flourat, A. L.; Allais, F.; Stavros, V. G. Gas-Solution Phase Transient Absorption Study of the Plant Sunscreen Derivative Methyl Sinapate. *ChemPhotoChem.* **2018**, *2*, 743–748.
- (16) Horbury, M. D.; Flourat, A. L.; Greenough, S. E.; Allais, F.; Stavros, V. G. Investigating isomer specific photoprotection in a model plant sunscreen. *Chem. Commun.* **2018**, *54*, 936–939.
- (17) Horbury, M. D.; Quan, W.-D.; Flourat, A. L.; Allais, F.; Stavros, V. G. Elucidating nuclear motions in a plant sunscreen during photoisomerization through solvent viscosity effects. *Phys. Chem. Chem. Phys.* **2017**, *19*, 21127–21131.
- (18) Zhao, X.; Luo, J.; Liu, Y.; Pandey, P.; Yang, S.; Wei, D.; Han, K. Substitution Dependent Ultrafast Ultraviolet Energy Dissipation Mechanisms of Plant Sunscreens. *J. Phys. Chem. Lett.* **2019**, *10*, 5244–5249.
- (19) Horbury, M. D.; Holt, E. L.; Mouterde, L. M. M.; Balaguer, P.; Cebrián, J.; Blasco, L.; Allais, F.; Stavros, V. G. Towards symmetry driven and nature inspired UV filter design. *Nat. Commun.* **2019**, *10*, 4748.
- (20) Sharma, A.; Bányiová, K.; Babica, P.; El Yamani, N.; Collins, A. R.; Cupr, P. Different DNA damage response of cis and trans isomers of commonly used UV filter after the exposure on adult human liver stem cells and human lymphoblastoid cells. *Sci. Total Environ.* **2017**, *593*, 18–26.
- (21) Peyrot, C.; Mention, M. M.; Brunissen, F.; Balaguer, P.; Allais, F. Innovative Bio-Based Organic UV-A and Blue Light Filters from Meldrum's Acid. *Molecules* **2020**, *25*, 2178.
- (22) Shaath, N. A. Ultraviolet filters. *Photochem. Photobiol. Sci.* **2010**, *9*, 464–469.
- (23) Diffey, B. A method for broad spectrum classification of sunscreens. *Int. J. Cosmet. Sci.* **1994**, *16*, 47–52.
- (24) Wang, S. Q.; Xu, H.; Stanfield, J. W.; Osterwalder, U.; Herzog, B. Comparison of ultraviolet A light protection standards in the United States and European Union through in vitro measurements of commercially available sunscreens. *J. Am. Acad. Dermatol.* **2017**, *77*, 42–47.
- (25) Diffey, B. The FDA final rule on labeling and effectiveness testing of sunscreens: Too little, too late? *J. Am. Acad. Dermatol.* **2012**, *66*, 162–163.
- (26) Snellenburg, J.; Laptinok, S.; Seger, R.; Mullen, K.; Van Stokkum, I. Glotaran: A Java-based graphical user interface for the R package TIMP. *J. Stat. Softw.* **2012**, *49*, 49.
- (27) Mullen, K. M.; Van Stokkum, I. H. M. TIMP: an R package for modeling multi-way spectroscopic measurements. *J. Stat. Softw.* **2007**, *18*, 1–46.
- (28) Tan, E. M. M.; Amirjalayer, S.; Bakker, B. H.; Buma, W. J. Excited state dynamics of Photoactive Yellow Protein chromophores elucidated by high-resolution spectroscopy and ab initio calculations. *Faraday Discuss.* **2013**, *163*, 321–340.
- (29) Kinoshita, S.-N.; Inokuchi, Y.; Onitsuka, Y.; Kohguchi, H.; Akai, N.; Shiraogawa, T.; Ehara, M.; Yamazaki, K.; Harabuchi, Y.; Maeda, S.; et al. The direct observation of the doorway  $1n\pi^*$  state of methylcinnamate and hydrogen-bonding effects on the photochemistry of cinnamate-based sunscreens. *Phys. Chem. Chem. Phys.* **2019**, *21*, 19755–19763.
- (30) Rodrigues, N. D. N.; Cole-Filipiak, N. C.; Turner, M. A.; Krokidi, K.; Thornton, G. L.; Richings, G. W.; Hine, N. D. M.; Stavros, V. G. Substituent position effects on sunscreen photodynamics: A closer look at methyl anthranilate. *Chem. Phys.* **2018**, *515*, 596–602.
- (31) Weersink, R. A.; Wallace, S. C. Complexes of Methyl 4-(N, N-Dimethylamino) benzoate: Spectroscopy and Dynamics of the Charge Transfer State. *J. Phys. Chem.* **1994**, *98*, 10710–10719.
- (32) Howell, R.; Phillips, D.; Petek, H.; Yoshihara, K. Fluorescence of jet-cooled dimethylamino benzonitrile, its aggregates and solvated complexes. *Chem. Phys.* **1994**, *188*, 303–316.
- (33) Baker, L. A.; Horbury, M. D.; Greenough, S. E.; Coulter, P. M.; Karsili, T. N. V.; Roberts, G. M.; Orr-Ewing, A. J.; Ashfold, M. N. R.; Stavros, V. G. Probing the ultrafast energy dissipation mechanism of the sunscreen oxybenzone after UVA irradiation. *J. Phys. Chem. Lett.* **2015**, *6*, 1363–1368.
- (34) Roberts, G. M.; Marroux, H. J. B.; Grubb, M. P.; Ashfold, M. N. R.; Orr-Ewing, A. J. On the participation of photoinduced N-H bond fission in aqueous adenine at 266 and 220 nm: a combined ultrafast transient electronic and vibrational absorption spectroscopy study. *J. Phys. Chem. A* **2014**, *118*, 11211–11225.
- (35) Horbury, M. D.; Baker, L. A.; Rodrigues, N. D. N.; Quan, W.-D.; Stavros, V. G. Photoisomerization of ethyl ferulate: A solution phase transient absorption study. *Chem. Phys. Lett.* **2017**, *673*, 62–67.